RSC Advances

PAPER

View Article Online
View Journal | View Issue

Cite this: *RSC Adv.*, 2020, **10**, 36949

Synthesis of Ni^{2+} ion doped ZnO–MWCNTs nanocomposites using an *in situ* sol–gel method: an ultra sensitive non-enzymatic uric acid sensing electrode material†

Sajid B. Mullani,[a] Anita K. Tawade,[c] Shivaji N. Tayade,[a] Kiran Kumar K. Sharma,[c] Shamkumar P. Deshmukh,[ab] Navaj B. Mullani,[d] Sawanta S. Mali,[e] Chang Kook Hong,[e] B. E. Kumara Swamy[f] and Sagar D. Delekar*[a]

Nickel (Ni^{2+}) ion doped zinc oxide-multi-wall carbon nanotubes (NZC) with different composition ratios of MWCNTs (from 0.01 to 0.1 wt%) are synthesized through an *in situ* sol–gel method. The synthesized NZC nanocomposites (NCs) are used as electrode materials with glassy carbon electrodes (GCEs) for electrochemical detection of uric acid (UA). The cyclic voltammogram of the representative NZC 0.1 modified GCE (NZC 0.1/GCE) revealed the highest electrochemical sensing activity towards the oxidation of UA at 0.37 V in 0.2 M phosphate buffer solution (PBS) having pH 7.4 ± 0.02. The limit of detection (LOD) and limit of quantification (LOQ) for the NZC 0.1/GCE are determined to be 5.72 nM and 19.00 nM (S/N = 3) respectively, which is the lowest compared to the literature values reported for enzymatic and non-enzymatic detection techniques. The synergistic effect of NZC 0.1 NCs is proposed as one of the factors for the enhanced electrochemical oxidation of UA complemented by the phase, lattice parameters, functional groups, morphology, elemental compositions, types of bonding and specific surface area with pore size ascertained using various techniques. The synthesized NZC 0.1 NCs are further proposed as selective electrode materials for the electrochemical detection of UA as authenticated further by performing interference tests with other metabolites such as ascorbic acid (AA), dopamine (DA) and D-glucose. The optimized electrochemical studies are further adopted for sensing of UA from human excretion samples using NZC 0.1 NCs.

Received 19th July 2020
Accepted 30th September 2020

DOI: 10.1039/d0ra06290a

rsc.li/rsc-advances

1. Introduction

Recently, semiconducting ternary nanocomposites (NCs) have played a vital role in various fields *viz.* energy harvesting, sensing, supercapacitors, catalysis, electronics, biomedical, *etc.*[1–4] Among these potential applications biosensing is a primary choice due the present need for precise identification, detection and quantification of metabolites in the complex biochemical processes of the human body and it provides a platform for easier, faster and accurate diagnosis of diseases.[5] In comparison to other metal oxides, nanocrystalline zinc oxide (ZnO) has been widely used in biosensing applications due to its biocompatibility, reasonable cost, low toxicity, high electron mobility, easy synthesis, large exciton binding energy (60 meV) at room temperature, higher chemical stability, *etc.*[6–8] To overcome these constraints, as well as to tune the properties of bare ZnO, investigators are continuously searching for different approaches such as, using binary NCs with other metal oxides[9] and with carbon nanostructures,[10–12] doping with metals[13,14] or non metals,[15,16] multicomponent hybrid systems[17–19] and supporting with metals.[20] Among these strategies, the focus on the doped as well as their binary/ternary ZnO-based NCs is gaining the importance due to their extraordinary properties compared to bare materials. Further, in connection to the enhancement in electrochemical properties, the NCs are to be prepared using highly conducting MWCNTs. Because the addition of MWCNTs, the charge transport properties as well as the stability of the host materials are enhanced which further, explored for sensors, supercapacitors, absorbent, photocatalytic,

[a]Department of Chemistry, Shivaji University, Kolhapur 416004, MS, India. E-mail: sddelekar7@rediffmail.com; Fax: +91 231 2692333; Tel: +91 231 2609311
[b]Department of Chemistry, D. B. F. Dayanand College of Arts and Science, Solapur 413002, MS, India
[c]School of Nanoscience and Biotechnology, Shivaji University, Kolhapur 416004, MS, India
[d]Department of Advanced Materials and Chemical Engineering, Hanyang University, ERICA, Ansan, 15588 South Korea
[e]Department of Advanced Chemical Engineering, Chonnam National University, Gwangju, 61186 South Korea
[f]Department of P.G. Studies and Research in Industrial Chemistry, Kuvempu University, Jnana Sahyadri, Shankaraghatta, Shimoga, Karnataka 577451, India

† Electronic supplementary information (ESI) available. See DOI: 10.1039/d0ra06290a

photovoltaic applications.[21,22] Particularly the use of MWCNTs in relation to electrochemical detection of biological samples and gases using sensors or biosensors[23] is multi-dimensions in terms of the sensitivity, selectivity, faster response and recovery.[24] Due to the well studied properties of binary ZnO–MWCNTs NCs, therefore there is still scope for further developments with the introduction of a suitable dopant in nanocrystalline ZnO host lattice. Hence, the synergetic of doping as well as the composites formations results ternary hybrid NCs; which offers the new insights into the host ZnO semiconductor for elevated biosensing performance of biological samples.

The research investigations are continuously going on the biosensing activity of ternary NCs. R. Saravanan *et al.* investigated the synthesis of ZnO and ZnO/Ag/Mn_2O_3 nanocomposite using vapor to solid mechanism using a facile thermal decomposition method and the overall synthesis protocol is tedious as well as costlier for sensing studies of uric acid (UA) and ascorbic acid (AA) sensing.[17] K. Ghanbari *et al.* designed the electrochemical deposition of ZnO flower-like/polyaniline nanofiber/reduced graphene oxide ternary nanocomposite on GCE. In this investigation, rGO was electrochemically reduced from the graphene oxide (GO) by applying a constant cathodic potential and after that *in situ* electrochemical synthesis of aniline monomer performed for preparing PANI/RGO nanocomposite. Thereafter, a modified electrode was prepared by electrochemical deposition of ZnO–metal nanoparticles (NPs) in over-oxidized polyaniline film modified GCE, but the electrode deposition by the nanocomposite and its are the main hurdles in the further development.[18] K. Ghanbari *et al.* investigated the ZnO–Cu_xO/polypyrrole nanocomposite modified electrode for simultaneous determination of AA, dopamine (DA) and UA. Initially, polypyrrole was electrochemically deposited on the GCE at ambient temperature and then it was further deposited with Cu_xO electrochemically. Thereafter, ZnO nanosheets cathodically deposited on the Cu_xO-PPy/GCE using aqueous solution of Zn $(NO_3)_2$ and KNO_3 electrolyte bath kept at 62 °C. In the present investigation, chemical stability of Cu_2O is one of the major issues and hence the present NCs would not be feasible for industrial scale applications. However, the limit of detection (LOD) value is higher than our present investigation and hence having limitation for sensing lower concentrations of an analytes.[19] Xuezhong Du *et al.* fabricated the sensitive electrochemical sensor using RGO supported Au@Pd (Au@Pd-RGO) NCs. In this present investigation, the synergetic of higher conductivity of RGO and surface area of the Au@Pd NPs resulting the higher sensitivity as well as selectivity of NCs for simultaneous determination of AA, DA and UA. However in the present investigation, high LOD and lower linear range of UA as well as very expensive metals are the major laggings in the NCs synthesis.[25] Hence, tedious protocol expensive material and sophisticated experimental approaches are the real constrains in the designing of ternary NCs. In addition, deposition of electrodes on the desired substrate and interconnectivity between the various components of the NCs are also further issues for getting the lower performance of sensing studies. Hence, to overcome these constraints, we deployed the simple, single step, wet chemical designing for the preparation of ternary NCs. During the present research endeavour, the proper connectivity between the different components as well as uniform, well adherent thin film deposition have been also focused very well. Therefore, the deposited NCs on GCE are showing the rapid and selective sensing activity of UA.

In connection to the doping studies; the introduction of appropriate metal ions in ZnO host lattice could bring significant changes in their sensing properties. Among the various dopants, Ni^{2+} is suitable dopant for ZnO related sensing applications because these ions have nearly same ionic radii (Ni^{2+} = 0.72 Å and Zn^{2+} = 0.74 Å) with same valence without changing in the overall structure properties, but resulting the enhanced the charge transport process useful for the electrochemical application.[26] Ni^{2+} ions doped ZnO materials have been reported for wide range of applications, but as per our best knowledge no one has been reported for biosensing applications.[27–30] Therefore, in present strategy, a combination of Ni^{2+} ions doped ZnO and MWCNTs will provide the required properties of an electrode material for biosensing studies.

In connection to biosensing measurement studies, various approaches are available to measure the content of UA levels; which also becomes the pre-requisite for proper diagnosis and prescription for the treatment of the various diseases related to UA. The various conventional clinical methods such as spectrophotometry, fluorometry, high-performance liquid chromatography (HPLC), capillary electrophoresis, liquid chromatography-mass spectrometry (LC-MS) *etc.* are used for the detection of UA.[31–37] But these techniques require sophisticated, expensive instruments, skilled manpower, time consuming accompanied by low specificity, large amount of sample. Hence, there is a need for new techniques which provides simple solutions to these shortcomings. Therefore, electrochemical based sensing is a promising portable method for a rapid and precise determination of electro-active metabolites like UA at μM concentration[38–40] due to their simple design, cost effectiveness, dynamic response, good selectivity, sensitivity *etc.*[41] The property of the electro-oxidizable UA is explored for the direct quantification through two methods *viz.* non-enzymatic and enzymatic methods. Among them, the non-enzymatic electrochemical sensing studies have the overriding advantages such as good sensitivity, free from enzyme activity, favorable stability, simple fabrication and spacious efforts.[42,43]

Therefore, in the present investigation, the NCs of Ni^{2+} ions doped ZnO NPs with MWCNTs have been chosen for non-enzymatic electrochemical sensing of UA. Further, the electrochemical sensing studies of NCs electrodes have been tested using the various parameters such as pH of buffer solution, concentration of UA, scan rate and interference from other metabolites and thereafter the optimized protocol has been used for sensing of UA from the real samples.

2. Experimental section

2.1 Synthesis of ZnO nanoparticles

The undoped ZnO NPs were prepared by using simple sol gel method. The desired amount of zinc acetate was dissolved in double distilled water (DDW). Aqueous solution of polyethylene

glycol (PEG) as a capping agent was dissolved in DDW separately added into the precursor solution with constant stirring. The pH of the solution was sustained up to 10.00 ± 0.02 using aqueous NaOH solution for the formation of gel. Afterwards, the solution was stirred for 3 h at room temperature. The obtained precipitate was filtered, washed with ethanol and dried in oven at 80 °C. The dried product calcinated in air at 400 °C for 2 h to form white crystalline powder of ZnO NPs.

2.2 Synthesis of nickel ions doped ZnO–MWCNTs nanocomposites

Nickel (Ni^{2+}) ions doped ZnO–MWCNTs NCs with varying content of MWCNTs (from 0.01 to 0.1 wt%) were prepared by simple *in situ* sol gel method. The acid-treated MWCNTs were dispersed separately in 10 mL of DDW by ultrasonication for 15 min. The desired amount of zinc acetate was dissolved in DDW and PEG used as a capping agent dissolved separately in DDW and then added into it with constant stirring. Afterwards 5 mol% of precursor of Ni added into above solution. Finally, dispersed solution of MWCNTs added into the running synthetic route of Ni^{2+} ions doped ZnO NPs after the gel formation. The pH of the resulting solution was adjusted to 10 ± 0.02 using NaOH solution. The solution is stirred for 5–6 h and allowed to cool to room temperature. The black precipitate was filtered, washed with ethanol and then dried in oven at 80 °C and calcinated in air at 400 °C for 2 h. The similar protocol followed for the synthesis of Ni^{+2} ions doped ZnO without addition of MWCNTs.

The prepared samples were labeled as ZnO NPs for ZnO; 5 NZ for 5 mol% Ni^{2+} ions doped ZnO and for Ni^{2+} ions doped ZnO NPs with MWCNTs as NZC 0.01, NZC 0.05, and NZC 0.1 with respect to the MWCNTs content of 0.01, 0.05 and 0.1 wt%, respectively.

2.3 Modification of glassy carbon electrode

Freshly prepared dispersions (1% w/v) of undoped ZnO NPs, 5 NZ or its NCs with MWCNTs (0.01 to 0.1 wt %) were prepared in ethanol. The dispersion was applied by drop casting on the GCE. The modified glassy carbon electrode was allowed to dry overnight in the vacuum desiccator.

3. Result and discussion

3.1 X-ray diffraction analysis

The crystal structure and the phase purity of the synthesized undoped, doped ZnO NPs, 5 NZ and NZC (0.01 to 0.1 wt %) NCs were investigated using powder X-ray diffraction (XRD). The XRD pattern of MWCNTs Fig. 1(a) shows a sharp peak at ~25.97° corresponding to a (002) reflection and its confirming the presence of elemental carbon (JCPDS no. 41-1487).[44,45] Fig. 1(b) includes the XRD patterns of the undoped ZnO NPs, 5 NZ and NZC (0.01, 0.05, 0.1) NCs. In undoped ZnO NPs, the XRD reflections (100), (002), (101), (102), (110), (103), (200), (112), (201) corresponds to 2θ values 31.78°, 34.44°, 36.27°, 47.54°, 56.60°, 62.87°, 66.49°,67.96°, 69.10° respectively revealing the presence of hexagonal wurtzite ZnO phase (JCPDS card 36-1451).[46,47] Absence of additional reflections confirm the absence of impurities Zn $(OH)_2$ or NiO like, which indicates the single-phase nature of the synthesized products and possible substitution of Ni^{2+} ions into the ZnO NPs host lattice.[48] The presence of sharp and intense peaks of the samples reveals the good crystalline nature having size range between 26 to 44 nm. Furthermore the most intense reflections of the 5 NZ and NZC NCs are slightly shifting to the lower angle to that of undoped ZnO NPs. Therefore, the observed result attributes the successful substitution of Ni^{2+} ions in host lattice of ZnO NPs.[49] While, in case of NZC NCs the characteristics XRD reflections of the ZnO NPs are retained in NCs at their respective 2θ values; without characteristics reflections corresponds to MWCNTs due to their less content or lower concentration of MWCNTs in the NCs and which could not be traced out by the XRD.[44]

In addition the close assessment of XRD patterns indicates that the intensity of XRD reflections are decreases significantly after forming NCs with MWCNTs upto NZC 0.1 NCs to that of undoped ZnO NPs. In case of 5 NZ the intensity of XRD reflections drastically reduced which is reported earlier[49,50] and if consider NZC NCs only, intensity of XRD pattern reflections is enhanced significantly from NZC 0.01 to NZC 0.05 NCs and

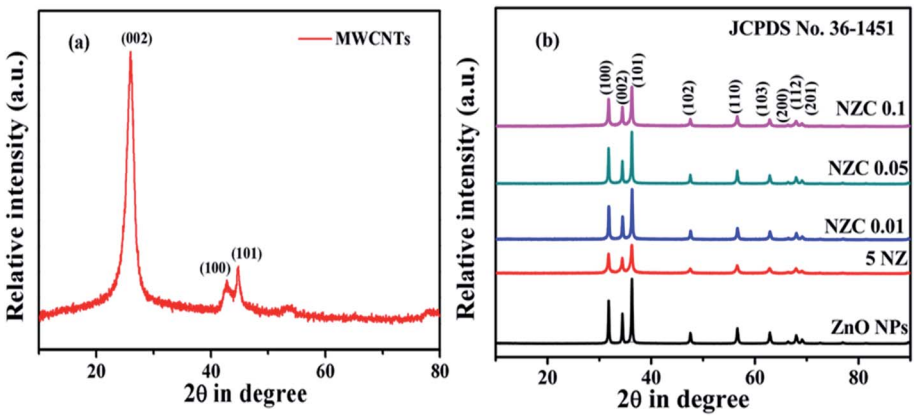

Fig. 1 XRD diffractograms of (a) MWCNTs (b) undoped ZnO NPs, 5 NZ and NZC NCs with varying content of MWCNTs (0.01 to 0.1 wt%).

Table 1 Observed structural cell parameters (XRD profile) of undoped ZnO NPs, 5 NZ and NZC NCs with varying content of MWCNTs (0.01 to 0.1 wt%)

Sample	Std. d. values (Å)	Obs. d. values (Å)	(*hkl*) plane	Cell parameters		
				a (Å)	*c* (Å)	*V* (A^3)
ZnO NPs	2.6033	2.6023	(002)	3.2488	5.2046	54.9329
	2.4759	2.4744	(101)			
	1.6247	1.6244	(110)			
5 NZ	2.6033	2.6050	(002)	3.2480	5.210	54.9629
	2.4759	2.4760	(101)			
	1.6247	1.6254	(110)			
NZC 0.01	2.6033	2.6006	(002)	3.2480	5.2012	54.8700
	2.4759	2.4728	(101)			
	1.6247	1.6240	(110)			
NZC 0.05	2.6033	2.6023	(002)	3.2502	5.2046	54.9803
	2.4759	2.4768	(101)			
	1.6247	1.6251	(110)			
NZC 0.1	2.6033	2.6023	(002)	3.2402	5.2046	54.6425
	2.4759	2.4752	(101)			
	1.6247	1.6251	(110)			

marginally decreases for NZC 0.1 NCs and this observation may highlight the limit of composition. The crystalline size can be estimated by Scherrer's formula,

$$D = \frac{0.9\lambda}{\beta \cos \theta} \quad (1)$$

The existence of MWCNTs in prepared material was further confirmed by the spectroscopic characterization tools *viz.*, FTIR, EDS and XPS analysis. The structural cell parameters of XRD patterns of the synthesized materials are reported in Table 1.

3.2 FTIR analysis

Fig. 2 displays the FTIR spectra of the undoped ZnO NPs, 5 NZ and NZC (0.01 to 0.1 wt %) NCs. FTIR spectrum of undoped ZnO NPs consists of characteristics transmission vibrational bands *viz.* 600–700 cm^{-1} due to Zn–O stretching mode.[51] The frequency region at 3000–3500 cm^{-1} corresponds due to the –OH functional moieties present in 5 NZ and NZC NCs.[44,52] In 5 NZ , sharp stretching bands observed at 830 cm^{-1},[51] 1066 cm^{-1} and 1378 cm^{-1} corresponding to the Zn–O–Ni bonding, Ni^{2+} ions occupies Zn^{2+} sites of host lattice of ZnO NPs and presence of NO_3.[53,54] The shift of stretching vibration frequencies of 5 NZ and NZC NCs as compare to undoped ZnO NPs with supporting of respective sharp stretching bands indicates the substitution of Ni^{2+} ions in Zn^{2+} sites of host lattice of ZnO NPs.[53]

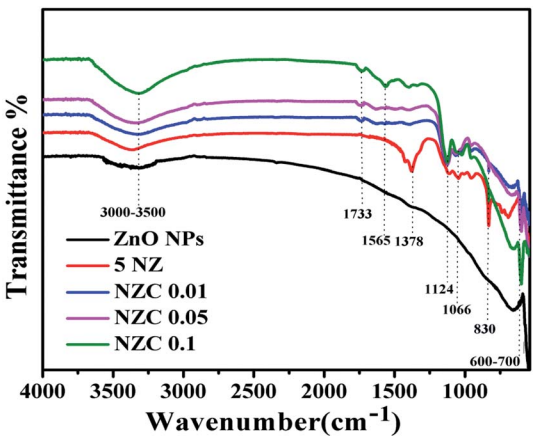

Fig. 2 FTIR spectra of undoped ZnO NPs, 5 NZ and NZC NCs with varying content of MWCNTs (0.01 to 0.1 wt%).

In FTIR patterns of the NZC NCs, along with the characteristics bands of ZnO and Ni, the additional bands are observed at bands observed at 1124 cm^{-1} corresponds to C–O (ester) stretching vibrations and 1565 cm^{-1}, 1733 cm^{-1} stretching vibrations corresponds to C=C (carbon–carbon bonding) of sidewall framework of MWCNTs, C=O (carboxylic acid) groups.[55] These peaks are very weak may be because of very low concentration variation of MWCNTs. Characteristics IR bands are slightly shifted in NZC NCs to that of undoped ZnO NPs. However, NZC NCs revealing the interconnectivity between the surface hydroxyl (–OH) functional group of ZnO NPs with acidic (–COOH) group of MWCNTs.

3.3. FESEM analysis

Fig. 3(a–e) shows the FESEM images of the undoped ZnO NPs, 5 NZ and its NCs with varying the content of MWCNTs (0.01 to 0.1 wt%). Surface morphological analysis of the prepared materials analyzed by FESEM. The FESEM images clearly show the variation in the morphology of the ZnO NPs due to Ni^{2+} doping without change its original crystal structure, indicating that the incorporation of Ni^{2+} influences the morphology of the ZnO NPs through its involvement during nucleation and grain growth. Observed results suggests that Ni^{2+} ions is replacing by Zn^{2+} in ZnO NPs and varying its morphology.[56] The varying content of MWCNTs in the Ni^{2+} ions doped ZnO NPs shown in Fig. 3(c–e) and it is demonstrates that Ni^{2+} ions doped ZnO NPs are densely covered the MWCNTs due to its very low concentration.

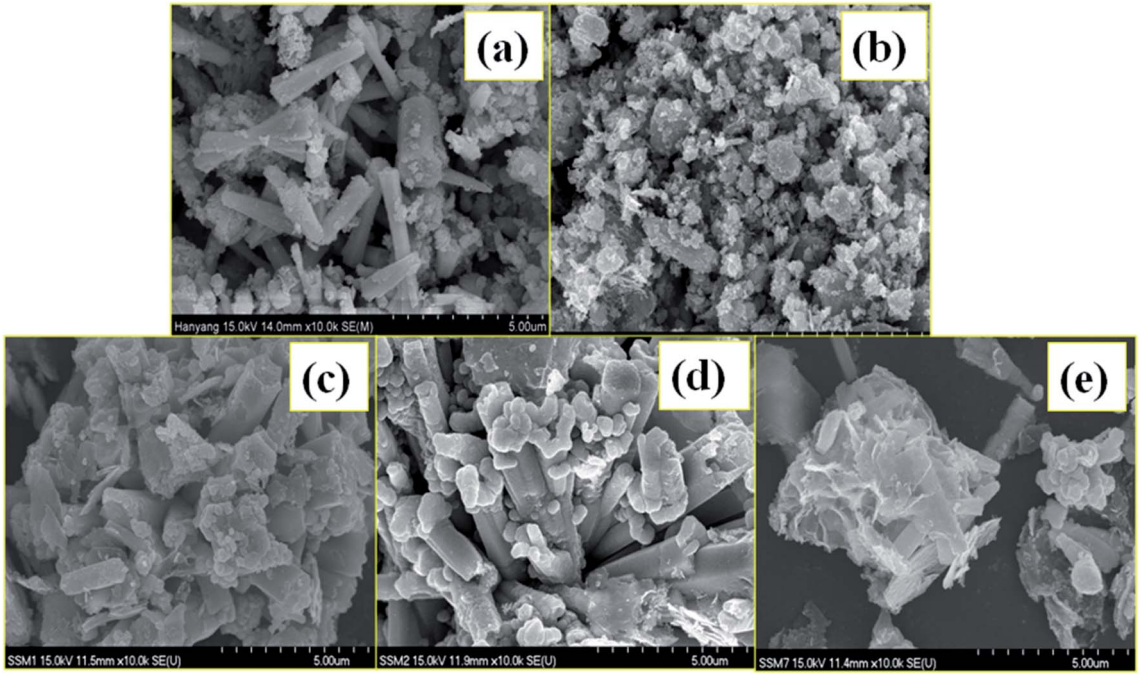

Fig. 3 FESEM images of the (a) undoped ZnO NPs (b) 5 NZ and (c–e) NZC NCs with varying content of MWCNTs (0.01 to 0.1 wt%).

3.4 EDS analysis

The elemental composition analysis of the undoped ZnO NPs, 5 NZ and its NCs with varying the content of MWCNTs (0.01 to 0.1 wt%) using EDS analysis and it is shown in Fig. 4(a–e) respectively. Fig. 4(a) shows the characteristics peaks of the elemental Zn and O and absent of the other peaks in the all patterns indicating no other impurities present in the undoped ZnO NPs. Also Fig. 4(b) confirms the existence of Ni with elemental Zn and O. Fig. 4(c–e) shows the existence of all the characteristics peaks corresponds to the elemental Zn, elemental O, elemental Ni as well as elemental C revealing the existence of all elements in the NZC NCs.

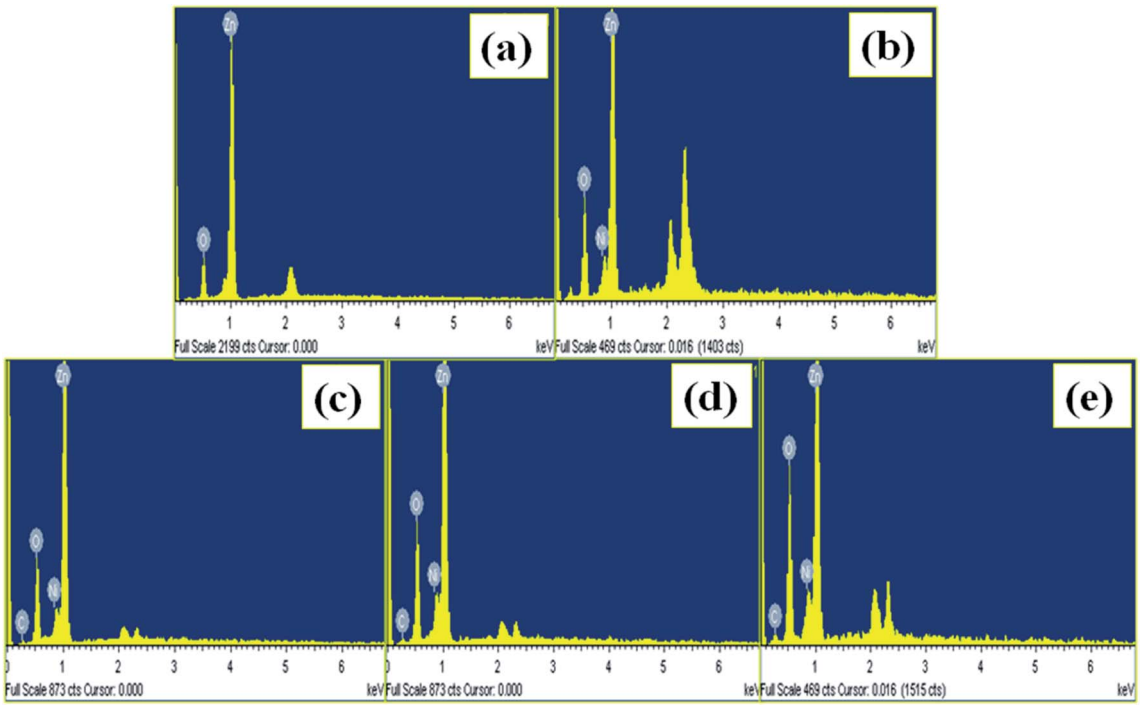

Fig. 4 EDS spectrums of the (a) undoped ZnO NPs (b) 5 NZ and (c–e) NZC NCs with varying content of MWCNTs (0.01 to 0.1 wt%).

3.5 TEM and HR-TEM with SAED analysis

Fig. 5 consists of TEM, HR-TEM and SAED images of synthesized samples. Fig. 5(a) TEM image displayed acid-modified MWCNTs without any NPs deposition reveals that the length of the MWCNTs are reduced after acid modification, since the mixed acid corroded and the functionalization decreases the weight of the MWCNTs and some defects along the side walls of the nanotubes. MWCNTs curled circular and entangled also occurred and some of them aggregated in bundles which were dispersed well in the matrix. HR-TEM *i.e.* Fig. 5(b) microphotographs of the acid-modified MWCNTs; demonstrate that the MWCNTs are straight. Acid-modified MWCNTs are straight and some of them aggregated in bundles and the outer diameter is 0.34 nm in size. The selected area electron diffraction (SAED) pattern [Fig. 5(c)] demonstrates the indexing of MWCNTs values are clearly matches with XRD value. Fig. 5(d–f) shows the TEM, HR-TEM image and SAED pattern of undoped ZnO NPs respectively. The TEM image clearly shows the particle sizes are in nanometer, from HR-TEM the lattice fringes width is 0.230 nm and it dominance of the (101) plane and this value closely matches with calculated *d* spacing values of XRD. The SAED pattern reveals distinct, clear and dotted pattern and it confirms the formation of ZnO NPs has single crystalline material in nature and indexing of SAED pattern of undoped ZnO NPs well matches with XRD data. Fig. 5(g–i) exhibits the TEM, HR-TEM and SAED pattern of NZC 0.1 NCs. The TEM and HR-TEM images, shows the Ni^{2+} ions doped ZnO anchored on the MWCNTs. In addition to this, in SAED pattern Fig. 5(i) demonstrate the formation of bright ring with clear dotted pattern confirms the deposited sample is polycrystalline in nature.

3.6 XPS analysis

(a) XPS analysis of ZnO NPs. The composition and chemical bond configuration of undoped ZnO NPs and representative NZC 0.1 NCs were analyzed by X-ray photoelectron spectroscopy (XPS). Fig. 6 demonstrates the high resolution XPS spectrum of the ZnO NPs at Zn 2p region and O 1s core level. Fig. 6(a) shows the typical XPS wide spectra of undoped ZnO NPs and it confirms the Zn and O present in synthesized material. The Zn 2p high resolution core-level of undoped ZnO NPs has two fitting peaks located at about 1044.60 and 1021.50 eV attributed to Zn $2p_{1/2}$ and Zn $2p_{3/2}$, respectively. Observed results indicate that the chemical valence of Zn is +2 in undoped ZnO NPs. The binding energy difference between the Zn $2p_{1/2}$ and Zn $2p_{3/2}$ is 23.1 eV which is good agreement with the energy splitting reported for ZnO NPs. Fig. 6(c) shows that the O 1s high resolution core-level spectrum of undoped ZnO NPs which shows three different forms of oxygen and it is centered at 532.98, 531.87 and 530.18 eV that binding energies can be ascribed to the adsorbed H_2O or O_2, O_2^- in the oxygen deficient regions and O_2^- ions in the wurtzite structure of ZnO NPs respectively.[57–59]

(b) XPS analysis of NZC 0.1 NCs. The elemental composition and states of the elemental species occurred in the NZC 0.1 NCs after the addition of Ni^{2+} ions doping in the NCs was confirmed by XPS analysis. Fig. 7(a) XPS survey spectrum of the NZC 0.1

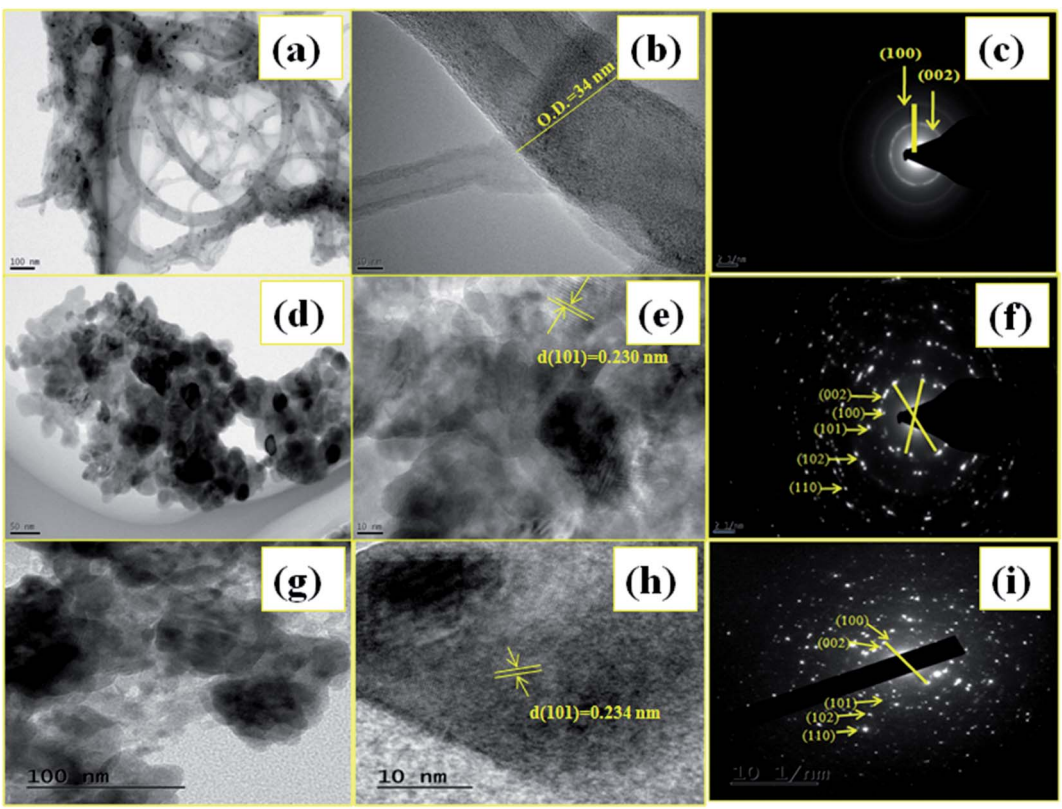

Fig. 5 TEM (a, d and g), HR-TEM (b, e and h) with SAED (c, f and i) patterns of MWCNTs, undoped ZnO NPs and representative NZC 0.1 NCs.

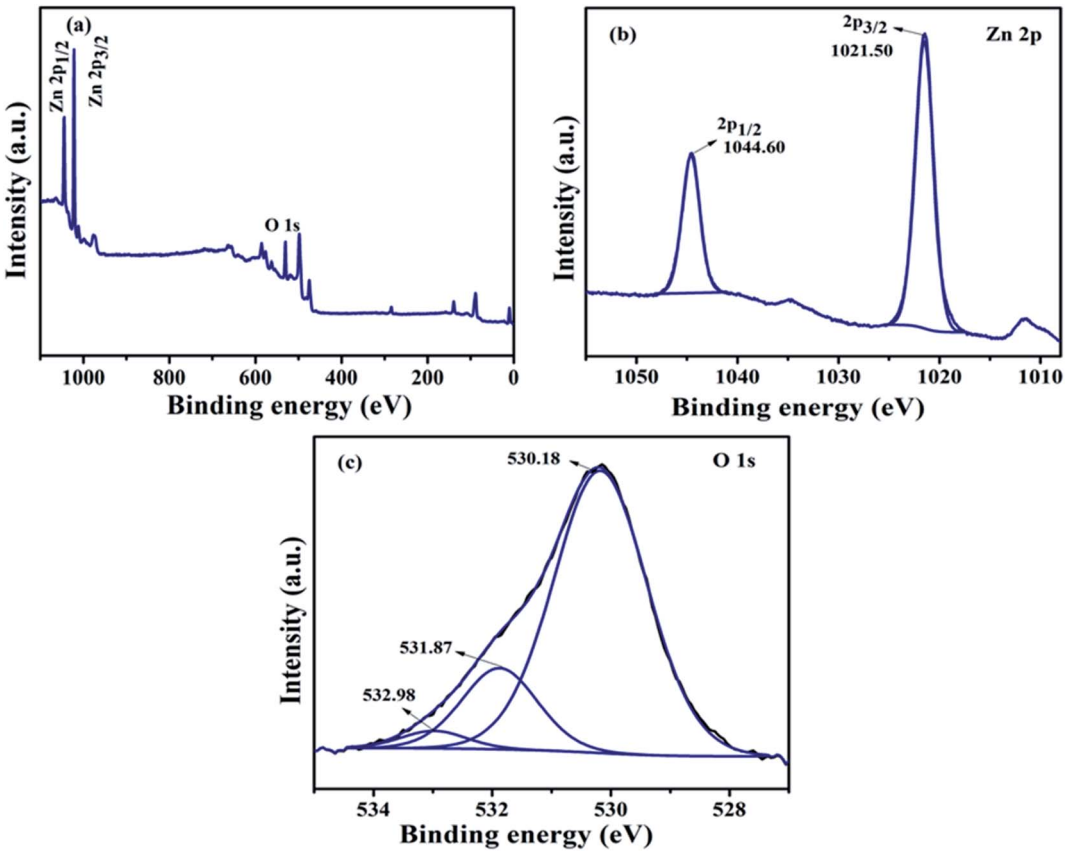

Fig. 6 (a) XPS survey spectrum and high resolution core level XPS spectrums of (b) Zn 2p and (c) O 1s of the undoped ZnO NPs.

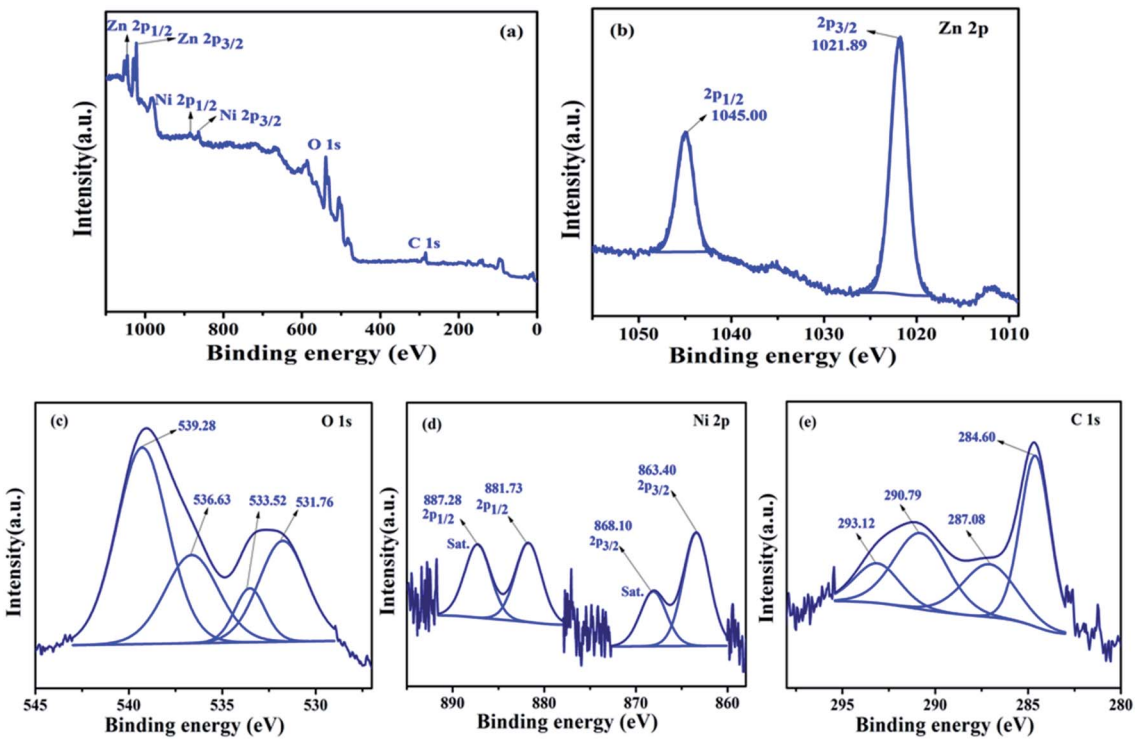

Fig. 7 (a) XPS survey spectrum and high resolution core level XPS spectrums of (b) Zn 2p (c) O 1s (d) Ni 2p and (e) C 1s of the representative NZC 0.1 NCs.

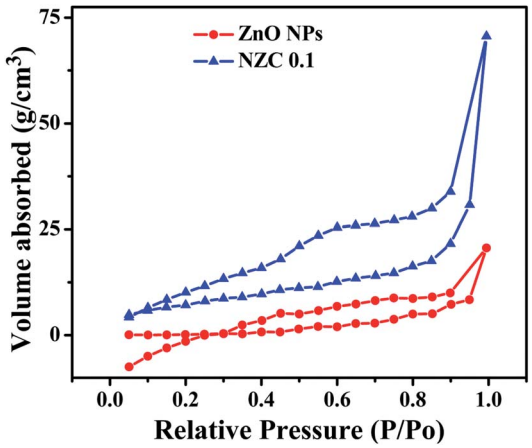

Fig. 8 N_2 adsorption–desorption isotherms of the undoped ZnO NPs and its representative NZC 0.1 NCs.

NCs. The observed peak in the survey spectrum concludes the existence of Zn, O, Ni and C and it is free from other elemental impurities. The corresponding binding energies conclude the well chemical connectivity between the components. Fig. 7(b) shows the Zn 2p spectrum and observed binding energy peaks at 1021.89 eV and 1045.00 eV are assigned to the Zn $2p_{3/2}$ and Zn $2p_{1/2}$ peaks of the Zn^{2+} and the difference between the Zn $2p_{3/2}$ and Zn $2p_{1/2}$ peaks is higher due to the slightly shifted towards higher binding energy as compare to undoped ZnO NPs (23.1 to 23.11 eV). This evidence confirms the formation of Zn–O–Ni bonding in the NZC 0.1 NCs and also confirming the existence of Ni^{2+} ions in synthesized materials.[47] High resolution O 1s spectrum [Fig. 7(c)] shows four deconvoluted peaks. The peak at 531.76 eV attributed to the OH^- (Ni). Along with, the binding energy at 533.52 eV is assigned to the characteristic of H_2O, which comes from crystal water and absorbed water from the air in samples[60] and 536.63 eV, 539.28 eV are assigned to the carbonated oxygen atom (–COOH). However in Ni 2p core level spectrum, [Fig. 7(d)] deconvoluted into two main peaks with binding energy at 863.40 eV and 881.73 eV and the corresponding satellite (Sat.) peaks at 868.10 eV and 887.28 eV were found, respectively and its characteristic for Ni^{2+} valence state as well as indicates that the Ni(II) present in NZC 0.1 NCs. The presence of Sat. peaks suggest the presence of a high-spin divalent state of Ni^{2+} in NCs, as probable for Ni^{2+} ions substituted at the Zn^{2+} sites of host lattice of ZnO NPs.[61] The presence of C in the NZC 0.1 NCs confirm by C 1s core level spectrum [Fig. 7(e)]. The high resolution spectrum of C 1s deconvoluted into four peaks. The high resolution scan of C 1s indicates the presence of sp^3 carbon at the binding energy of 284.6 eV, as expected and remaining peaks at 287.08, 290.79 and 293.12 eV assigned to the carbon based functional moieties of MWCNTs incorporated with Ni^{2+} ions doped ZnO NPs such as, C–C, C=O and O=C–O respectively.[62–64]

3.7 Brunauer–Emmett–Teller (BET) surface area analysis

To investigate the specific areas and the porous nature of the undoped ZnO NPs and representative NZC 0.1 NCs, Brunauer–Emmett–Teller (BET) measurements were performed. Fig. 8 depicts N_2 adsorption–desorption isotherms of the undoped ZnO NPs and representative NZC 0.1 NCs.

Table 2 Specific surface, pore volume and pore size from BET analysis of representative undoped ZnO NPs, and NZC 0.1 NCs

Sample	Specific surface area ($m^2\ g^{-1}$)	Pore volume ($cm^3\ g^{-1}$)	Pore size (nm)
ZnO NPs	14.448	0.035	3.420
NZC 0.1	33.192	0.101	3.828

Also, the total pore volume and average pore diameter of the samples were investigated by using the Barrett–Joyner–Halenda (BJH) method. Both the samples display the type IV curve accompanied by a type H3 hysteresis loop and according to the IUPAC classification, predominance of mesoporous (pores 2–50 nm diameter).[65] BET surface areas of undoped ZnO NPs and representative NZC 0.1 NCs was examined to be 14.448 and 33.192 $m^2\ g^{-1}$ respectively (Table 2). These BET analysis indicated that NZC 0.1 NCs attributes higher surface area with better mesoporous structure, which is appropriate for improved sensing performance.

3.8 EIS analysis

The redox electrochemical impedance spectroscopy (EIS) study has been carried out to monitor the electron transfer resistance

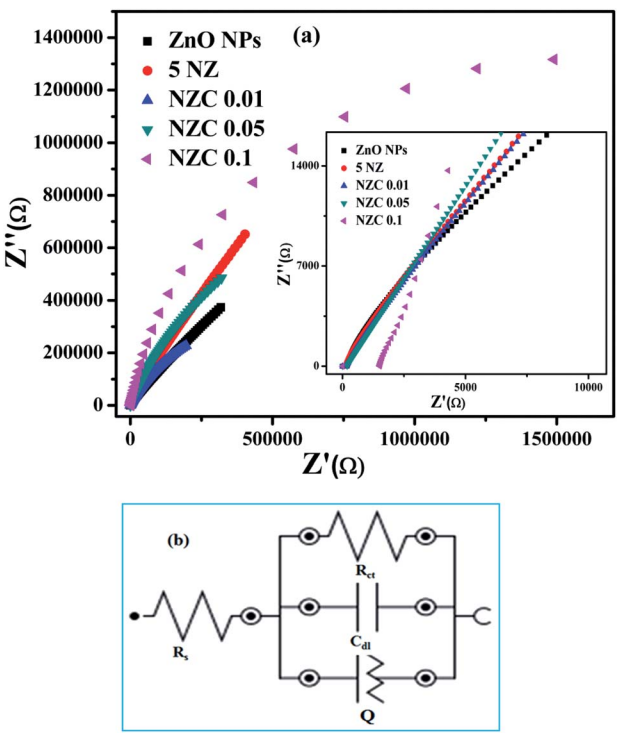

Fig. 9 (a) Electrochemical impedance spectroscopy (EIS) Nyquist plots of undoped ZnO NPs, 5 NZ and NZC (0.01, 0.05, 0.1) NCs in 5 mM K_3 [Fe(CN)$_6$] in 0.1 M PBS (pH 7.4) *vs.* Ag/AgCl electrode and (b) model circuit used for fitting the impedance data.

Table 3 Charge transfer resistance (R_{ct}) values for the modified electrodes in 5 mM ferrocene in 0.1 M PBS (pH 7.4) *vs.* Ag/AgCl electrode

Electrode	R_{ct} (MΩ)	Error
GCE/ZnO NPs	8.89	±0.55
GCE/5 NZ	1.10	±2.81
GCE/NZC 0.01	1.68	±0.45
GCE/NZC 0.05	2.46	±0.93
GCE/NZC 0.1	1.07	±1.68

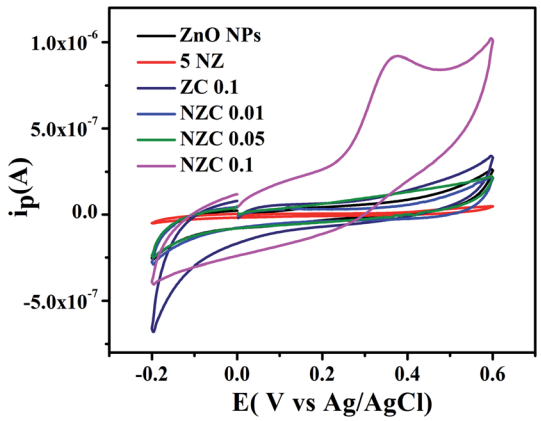

Fig. 10 Cyclic voltammograms of undoped ZnO NPs, 5 NZ, ZC 0.1 and NZC NCs with 25 × 10^{-4} M UA in 0.2 M PBS (pH 7.4) at 50 mV S^{-1}.

between the modified GCE and electrolyte (ferrocene redox couple). The impedance spectra (Nyquist plots) obtained for the electrodes are presented in Fig. 9(a). While Fig. 9(b) shows the equivalent circuit used to fit impedance data.

The measured EIS data fitted using NOVA 2.1.4 software to obtain the charge transfer resistance (R_{ct}) of the modified GCE. The respective R_{ct} values are represented in the Table 3. According to the EIS results, NZC 0.1/GCE electrode exhibit a nearly straight line with significantly lower charge transfer resistance (R_{ct}) value interface with ferrocene (1.07 MΩ).

Observed results suggests that synthesized NZC 0.1 NCs enhanced electrochemical process of the electrode and electrolyte interface in contrast to a relatively slow electrochemical performance of undoped ZnO NPs, 5 NZ and NZC (0.01, 0.05) NCs. Therefore, from the EIS data, NZC 0.1/GCE shows lowest R_{ct} value for efficient charge transfer at the electrode. The low R_{ct} indicates the NZC 0.1 NCs possess high electrical conductivity and helps to enhance the electrochemical sensing activity at the surface of the NZC 0.1/GCE modified electrode.

3.9 Electrochemical study of uric acid using cyclic voltammetry technique

The GCE are modified with 1 mg mL^{-1} of the synthesized undoped ZnO NPs, 5 NZ, ZC 0.1 and NZC (0.01 to 0.1 wt%) NCs. The electrochemical sensing activity measurements were carried out in 0.2 M PBS (pH 7.4) with potential window −0.2 to 0.6 V. The UA oxidation at undoped ZnO NPs, 5 NZ, ZC 0.1 and NZC (0.01, 0.05, 0.1) NCs modified electrodes by CV measurements were conducted. Fig. 10 displays the comparative overlay CV results of UA at modified GCE. The electrochemical performance of modified electrodes in 0.2 M PBS (pH 7.4) (scan rate 50 mV s^{-1} and 25 × 10^{-4} M UA) with potential window −0.2 to 0.6 V for the NZC 0.1/GCE modified electrode exhibited a significant hike in the anodic peak as compared to other modified GCE. However NZC 0.1/GCE shows oxidation peak potential at 0.37 V with highest current response. This is attributed to the larger surface area of NZC 0.1/GCE and enhanced electron transfer rate. The results suggest, NZC 0.1/GCE NCs exhibits efficient electrochemical activity for UA. This is consistent with the higher charge transfer as observed in EIS studies [Fig. 9(a)] and high surface area of NZC 0.1 NCs.

(a) Effect of concentration. To investigate the effect of concentration (0–625 nM) were added into the 0.2 M PBS at pH 7.4 and applied potential window −0.2 to 0.6 V with scan rate 50 mV s^{-1}. The current response of the NZC 0.1/GCE modified electrode to consecutive increase in the concentration from 6.25 to 625 nM UA is investigated by CV in 0.2 M PBS of 40 mL at pH 7.4. The cyclic voltammograms are shown in Fig. 11(a) which depicts the oxidation current at 0.37 V increases with addition

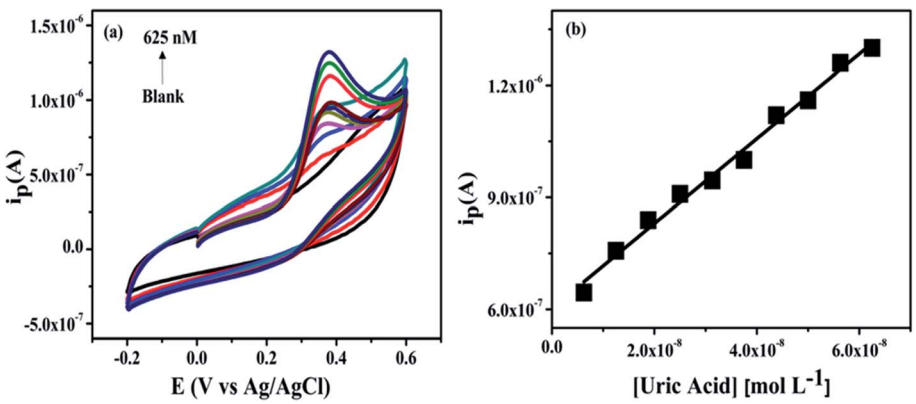

Fig. 11 Cyclic voltammograms of various concentration of UA in 0.2 M PBS (6.25 to 625 nM) at pH 7.4 (a) and the calibration curve of oxidation peak current *vs.* concentration (b).

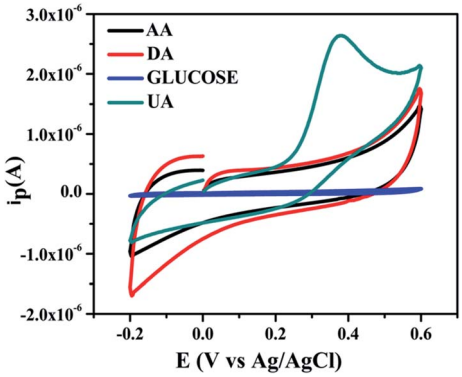

Fig. 12 Interference test of NZC 0.1/GCE in 0.2 M 7.4 phosphate buffer 50 mV s^{-1} with 25 × 10^{-4} M UA in the presence of 0.05 mM of AA, DA and D-glucose respectively.

of UA upto 625 nM. Fig. 11(b) shows the dependence of the anodic peak current (I_{pa}) with increasing UA concentration from 6.25 nM to 625 nM. Based on the I_{pa}, the sensor calibration is performed three times and the standard deviations are calculated. The value of I_{pa} obtained from the linear plot in Fig. 11(b) is further used for the calculation of the limit of detection (LOD) and limit of quantification (LOQ).

The linear equation is I_{pa} = (1.3616 × 10^{-6} C + 3.6819 × 10^{-7}) (R^2 = 0.98) and LOD, LOQ in 0.2 M PBS (pH 7.4) are calculated from the following equations,

$$\mathrm{LOD} = 3\mathrm{SD}/b \quad (2)$$

$$\mathrm{LOQ} = 10\mathrm{SD}/b \quad (3)$$

where, SD is the standard deviation of the blank solution and b is the slope of the analytical curve. The LOD and LOQ (S/N = 3) are calculated to be 5.72 nM and 19 nM respectively, which is lowest as compared to literature values reported so far [Table S1 (ESI†)].

(b) Interference test. The selectivity of designed the sensor is crucial parameter in terms of clinical applicability. Therefore, the interference test was also tested of NZC 0.1/GCE modified electrode. For this purpose, 0.05 mM of AA, DA and D-glucose was added into 25 × 10^{-4} M UA. The interference test was performed into 0.2 M 7.4 phosphate buffer at 50 mV s^{-1} scan rate for NZC 0.1/GCE modified electrode. Fig. 12 depicts cyclic voltammograms of the interference test of the designed sensor NZC 0.1/GCE with respect to different interfering biomolecules such as AA, DA and D-glucose.

From the experimentally obtained cyclic voltammograms, it shows no responsive signals for the AA, DA and D-glucose thus, no interference response on the redox behavior of UA at the NZC 0.1/GCE. Therefore, we conclude that NZC 0.1/GCE highly selective towards the detection of UA only. The employed NZC 0.1/GCE sensor exhibit high sensitivity and selectivity for UA. Further, this indicates that presence of minimum oxidation energy barrier to oxidation of UA without interfering species.

(c) Effect of pH. In most cases, pH of the electrolyte (PBS) plays an important influence factor to the electrochemical reaction. The effect of varying of pH (3–10) (*i.e.* acidic, basic and neutral condition) towards electrochemical activity of UA is investigated to optimize the pH condition of the biosensor. Fig. 13(a) shows anodic peak current gradually increasing with increasing pH up to 3–6 and 8–10 with slight potential shift but peak current increased drastically at pH 7.4. However, as the pH of the PBS solution increased from 3 to 10, the peak potential is shifted towards negatively potential which illustrates that protons are involved in the UA oxidation processes at the modified GCE electrode surface.[66] Further, a plot of peak current *vs.* pH as shown in Fig. 13(b), displays maximum anodic current of UA at pH 7.4. Therefore, pH 7.4 is optimized for further electrochemical detection of UA.

(d) Effect of scan rate. The effect of the scan rate on the electrochemical behavior of NZC 0.1/GCE with UA 25 × 10^{-4} M in 0.2 M PBS (pH = 7.4) studied by varying the scan rate from 10–100 mV s^{-1} and are depicted in Fig. 14(a). The oxidation peak current was found to increase linearly with the increase in the scan rate as shown in Fig. 14(b). This attributes to diffusion controlled process of the UA oxidation on the electrode. The diffusion coefficient of the UA found to be 0.16 × 10^{-6} cm^2 s^{-1}. The active surface area of the NZC 0.1/GCE modified electrode

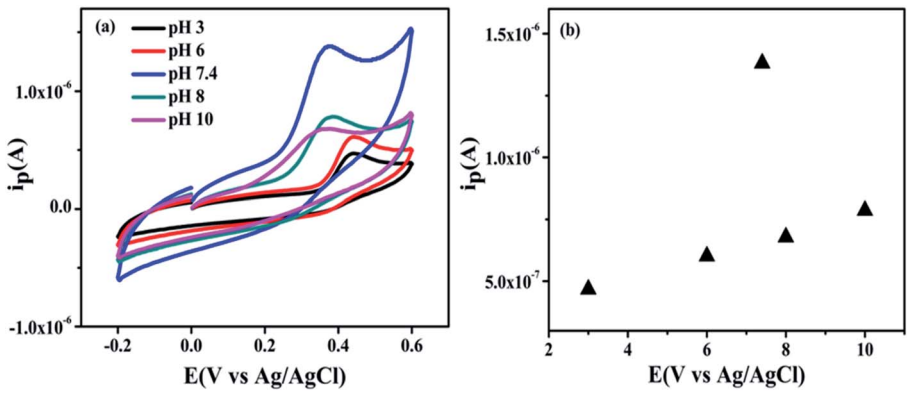

Fig. 13 (a) Cyclic voltammograms shows effect of different pH solutions (3–10) with 25 × 10^{-4} M UA with NZC 0.1/GCE in 0.2 M PBS at a scan rate of 50 mV S^{-1} (b) plot between current *vs.* pH.

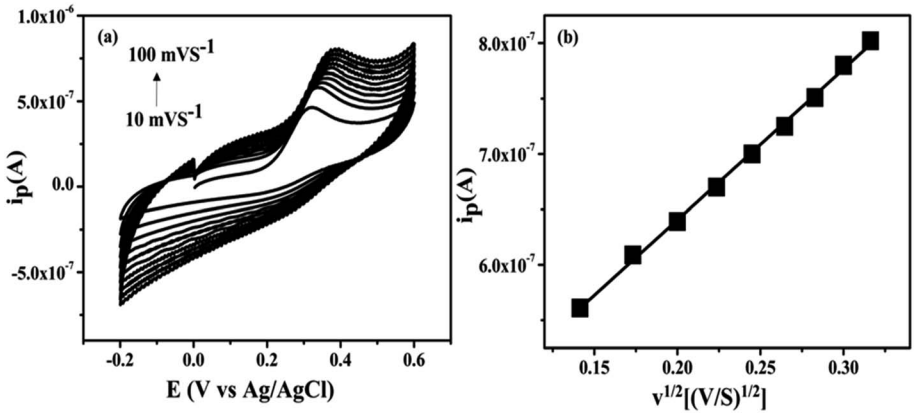

Fig. 14 (a) Cyclic voltammetry curves at NZC 0.1/GCE in 25 × 10^{-4} M UA in 0.2 M PBS (pH 7.4) at different scan rates (from 10 to 100 mV s^{-1}) (b) peak current *vs.* scan rate.

Table 4 Recovery study of UA at the NZC 0.1/GCE modified electrode

Sample	Added (μM)	Found (μM)	Recovery	RSD (%)
1	1.00 × 10^{-4}	1.00 × 10^{-4}	100	26.6
2	1.40 × 10^{-4}	1.41 × 10^{-4}	100.7	18.9
3	1.50 × 10^{-4}	1.50 × 10^{-4}	100	17.7
Standard deviation 2.67 × 10^{-7}				

was determined (0.15 cm^2) using the literature value of diffusion coefficient (0.16 × 10^{-6} cm^2 s^{-1}) of the ferrocene.[67]

3.10 Determination of uric acid in human urine sample

The recovery study for UA oxidation was carried out at the NZC 0.1/GCE modified electrode in 0.2 M PBS (pH 7.4). Urine samples were collected from three volunteers. The recovery results are shown in Table 4. The analysis was carried out by differential pulse voltammetry (DPV), with the addition of UA in each sample respectively as depicted in Table 4.

The RSD values were calculated by taking three measurements of each sample and average of calculated using the following relationship. The found values were reported Table 4. The % RSD values were calculated using following relationship.

$$\text{RSD } (\%) = \frac{\text{standard deviation in found concentration}}{\text{found concentration}} \times 100$$

Thus, proposed sensor showed great potential for the determination of UA from human urine samples.

4. Conclusion

In present work demonstrates a successful synthesis of Ni^{2+} ion doped ZnO–MWCNTs nanocomposites. The electrochemical sensing activity of NZC 0.1/GCE for the oxidation of UA at 0.37 V at pH 7.4. The fabricated electrode NZC 0.1/GCE showed ultra-sensitivity for UA corresponding to LOD of 5.72 nM and LOQ of 19.00 nM. The selectivity of NZC 0.1/GCE to UA in presence of other biological metabolite species such *viz.* D-glucose, DA and AA is very significant. The fabricated electrode showed exceptionally high sensitivity compared with the existing enzyme immobilized UA sensors. The recovery test using human urine is encouraging. Overall, the fabricated NZC 0.1/GCE electrode is ultra-sensitive, stable, efficient recovery and reproducibility for UA detection owing to incorporation of Ni^{2+} ions. This fabricated electrode has potential for an ultra-sensitive UA sensor.

Conflicts of interest

There are no conflicts of interest to declare.

Acknowledgements

Author SBM, gratefully acknowledge to University Grants Commission, New Delhi for financial support under Basic Scientific Research scheme (UGC No. F.25-1/2014-15(BSR)/7-183/2009(BSR)-5 Nov. 2015).

References

1 X. Liu, J. Iocozzia, Y. Wang, X. Cui, Y. Chen, S. Zhao, Z. Li and Z. Lin, *Energy Environ. Sci.*, 2017, **10**, 402–434.
2 H. Huo, C. Guo, G. Li, X. Han and C. Xu, *RSC Adv.*, 2014, **4**, 20459–20465.
3 W. Wu, L. Yang, S. Chen, Y. Shao, L. Jing, G. Zhao and H. Wei, *RSC Adv.*, 2015, **5**, 91645–91653.
4 Y. Liu, J. Huang and H. Li, *J. Mater. Chem. B*, 2013, **1**, 1826–1834.
5 P. Chandra, Y. N. Tan and S. P. Singh, *Next generation point-of-care biomedical sensors technologies for cancer diagnosis*, Springer, 2017.
6 A. B. Djurišić, X. Chen, Y. H. Leung and A. M. C. Ng, *J. Mater. Chem.*, 2012, **22**, 6526–6535.
7 F. De Angelis and L. Armelao, *Phys. Chem. Chem. Phys.*, 2011, **13**, 467–475.

8 A. K. Panigrahi, V. Singh and S. G. Singh, *Analyst*, 2017, **142**, 2128–2135.
9 C. Zhou, L. Xu, J. Song, R. Xing, S. Xu, D. Liu and H. Song, *Sci. Rep.*, 2014, **4**, 7382.
10 M. Tak, V. Gupta and M. Tomar, *J. Mater. Chem. B*, 2013, **1**, 6392–6401.
11 K. Zhao, X. Yan, Y. Gu, Z. Kang, Z. Bai, S. Cao, Y. Liu, X. Zhang and Y. Zhang, *Small*, 2016, **12**, 245–251.
12 P. Nayak, B. Anbarasan and S. Ramaprabhu, *J. Phys. Chem. C*, 2013, **117**, 13202–13209.
13 S. Das, S. Mukhopadhyay, S. Chatterjee, P. S. Devi and G. Suresh Kumar, *ACS Omega*, 2018, **3**, 7494–7507.
14 C. Yang, C. Xu and X. Wang, *Langmuir*, 2012, **28**, 4580–4585.
15 N. Muthuchamy, R. Atchudan, T. N. J. I. Edison, S. Perumal and Y. R. Lee, *J. Electroanal. Chem.*, 2018, **816**, 195–204.
16 K. Jindal, M. Tomar and V. Gupta, *Analyst*, 2013, **138**, 4353–4362.
17 R. Saravanan, M. M. Khan, V. K. Gupta, E. Mosquera, F. Gracia, V. Narayanan and A. Stephen, *RSC Adv.*, 2015, **5**, 34645–34651.
18 K. Ghanbari and M. Moloudi, *Anal. Biochem.*, 2016, **512**, 91–102.
19 K. Ghanbari and N. Hajheidari, *Anal. Biochem.*, 2015, **473**, 53–62.
20 D. Pradhan, F. Niroui and K. Leung, *ACS Appl. Mater. Interfaces*, 2010, **2**, 2409–2412.
21 R. Alshehri, A. M. Ilyas, A. Hasan, A. Arnaout, F. Ahmed and A. Memic, *J. Med. Chem.*, 2016, **59**, 8149–8167.
22 S. Mallakpour and E. Khadem, *Chem. Eng. J.*, 2016, **302**, 344–367.
23 N. G. Mphuthi, A. S. Adekunle and E. E. Ebenso, *Sci. Rep.*, 2016, **6**, 26938.
24 I. Zaporotskova, N. Boroznina, Y. Parkhomenko and L. Kozhitov, *Mod. Electron. Mater.*, 2016, **2**(4), 95–105.
25 J. Jiang and X. Du, *Nanoscale*, 2014, **6**, 11303–11309.
26 M. Tak, V. Gupta and M. Tomar, *J. Electroanal. Chem.*, 2017, **792**, 8–14.
27 J. H. He, C. S. Lao, L. J. Chen, D. Davidovic and Z. L. Wang, *J. Am. Chem. Soc.*, 2005, **127**, 16376–16377.
28 R. Saravanan, K. Santhi, N. Sivakumar, V. Narayanan and A. Stephen, *Mater. Charact.*, 2012, **67**, 10–16.
29 N. V. Kaneva, D. T. Dimitrov and C. D. Dushkin, *Appl. Surf. Sci.*, 2011, **257**, 8113–8120.
30 H. Colder, E. Guilmeau, C. Harnois, S. Marinel, R. Retoux and E. Savary, *J. Eur. Ceram. Soc.*, 2011, **31**, 2957–2963.
31 D. L. Rocha and F. R. Rocha, *Microchem. J.*, 2010, **94**, 53–59.
32 N. E. Azmi, N. I. Ramli, J. Abdullah, M. A. A. Hamid, H. Sidek, S. A. Rahman, N. Ariffin and N. A. Yusof, *Biosens. Bioelectron.*, 2015, **67**, 129–133.
33 D. Swinson, J. Snaith, J. Buckberry and M. Brickley, *Int. J. Osteoarchaeol.*, 2010, **20**, 135–143.
34 W. Pormsila, S. Krähenbühl and P. C. Hauser, *Anal. Chim. Acta*, 2009, **636**, 224–228.
35 X. Dai, X. Fang, C. Zhang, R. Xu and B. Xu, *J. Chromatogr. B: Anal. Technol. Biomed. Life Sci.*, 2007, **857**, 287–295.
36 W. Kwon, J. Y. Kim, S. Suh and M. K. In, *Forensic Sci. Int.*, 2012, **221**, 57–64.
37 S. N. Tayade, A. K. Tawade, P. Talele, S. S. Chavan and K. K. Sharma, *Methods Appl. Fluoresc.*, 2019, **7**, 045002.
38 K. Mahato, P. K. Maurya and P. Chandra, *3 Biotech*, 2018, **8**, 149.
39 P. E. Erden and E. Kılıç, *Talanta*, 2013, **107**, 312–323.
40 S. Verma, J. Choudhary, K. P. Singh, P. Chandra and S. P. Singh, *Int. J. Biol. Macromol.*, 2019, **130**, 333–341.
41 A. G. Theakstone, E. H. Doeven, X. A. Conlan, L. Dennany and P. S. Francis, *Chem. Commun.*, 2019, **55**, 7081–7084.
42 X. Niu, X. Li, J. Pan, Y. He, F. Qiu and Y. Yan, *RSC Adv.*, 2016, **6**, 84893–84905.
43 Z. Xu, M.-q. Zhang, H.-q. Zou, J.-s. Liu, D.-z. Wang, J. Wang and L.-d. Wang, *J. Electroanal. Chem.*, 2019, **841**, 129–134.
44 S. D. Delekar, A. G. Dhodamani, K. V. More, T. D. Dongale, R. K. Kamat, S. F. Acquah, N. S. Dalal and D. K. Panda, *ACS Omega*, 2018, **3**, 2743–2756.
45 M.-M. Lu, W.-Q. Cao, H.-L. Shi, X.-Y. Fang, J. Yang, Z.-L. Hou, H.-B. Jin, W.-Z. Wang, J. Yuan and M.-S. Cao, *J. Mater. Chem. A*, 2014, **2**, 10540–10547.
46 I. Balti, A. Mezni, A. Dakhlaoui-Omrani, P. Leone, B. Viana, O. Brinza, L.-S. Smiri and N. Jouini, *J. Phys. Chem. C*, 2011, **115**, 15758–15766.
47 J. Cui, J. Jiang, L. Shi, F. Zhao, D. Wang, Y. Lin and T. Xie, *RSC Adv.*, 2016, **6**, 78257–78263.
48 R. S. Kumar, S. Dananjaya, M. De Zoysa and M. Yang, *RSC Adv.*, 2016, **6**, 108468–108476.
49 K. Barick, M. Aslam, V. P. Dravid and D. Bahadur, *J. Phys. Chem. C*, 2008, **112**, 15163–15170.
50 Q. Yin, W. Wu, R. Qiao, X. Ke, Y. Hu and Z. Li, *RSC Adv.*, 2016, **6**, 38653–38661.
51 N. Goswami and A. Sahai, *Mater. Res. Bull.*, 2013, **48**, 346–351.
52 D. Verma, V. Sharma, G. Okram and S. Jain, *Green Chem.*, 2017, **19**, 5885–5899.
53 I. B. Elkamel, N. Hamdaoui, A. Mezni, R. Ajjel and L. Beji, *RSC Adv.*, 2018, **8**, 32333–32343.
54 M. Y. Ghotbi, *Particuology*, 2012, **10**, 492–496.
55 M. J. Yee, N. Mubarak, M. Khalid, E. Abdullah and P. Jagadish, *Sci. Rep.*, 2018, **8**, 1–16.
56 A. K. Rana, Y. Kumar, P. Rajput, S. N. Jha, D. Bhattacharyya and P. M. Shirage, *ACS Appl. Mater. Interfaces*, 2017, **9**, 7691–7700.
57 I. A. Hassan, S. Sathasivam, S. P. Nair and C. J. Carmalt, *ACS Omega*, 2017, **2**, 4556–4562.
58 J. Wang, Y. Li, Y. Kong, J. Zhou, J. Wu, X. Wu, W. Qin, Z. Jiao and L. Jiang, *RSC Adv.*, 2015, **5**, 81024–81029.
59 X. Cai, Y. Cai, Y. Liu, H. Li, F. Zhang and Y. Wang, *J. Phys. Chem. Solids*, 2013, **74**, 1196–1203.
60 J. Hao, X. Wang, F. Liu, S. Han, J. Lian and Q. Jiang, *Sci. Rep.*, 2017, **7**, 3021.
61 X. Huang, G. Li, B. Cao, M. Wang and C. Hao, *J. Phys. Chem. C*, 2009, **113**, 4381–4385.
62 S. R. Ede, S. Anantharaj, K. Kumaran, S. Mishra and S. Kundu, *RSC Adv.*, 2017, **7**, 5898–5911.
63 A. E. Vilian, V. Veeramani, S.-M. Chen, R. Madhu, C. H. Kwak, Y. S. Huh and Y.-K. Han, *Sci. Rep.*, 2015, **5**, 18390.

64 G. An, P. Yu, M. Xiao, Z. Liu, Z. Miao, K. Ding and L. Mao, *Nanotechnology*, 2008, **19**, 275709.
65 X. Xiao, B. Han, G. Chen, L. Wang and Y. Wang, *Sci. Rep.*, 2017, **7**, 40167.
66 S. Shahrokhian, M. Ghalkhani and M. K. Amini, *Sens. Actuators, B*, 2009, **137**, 669–675.
67 B. B. Kamble, M. Naikwade, K. Garadkar, R. B. Mane, K. K. K. Sharma, B. D. Ajalkar and S. N. Tayade, *J. Mater. Sci.: Mater. Electron.*, 2019, **30**, 13984–13993.